Nanoscale

Accepted Manuscript

This article can be cited before page numbers have been issued, to do this please use: T. Wang, Q. Yu, S. Zhang, X. Kou, P. Sun and G. Lu, *Nanoscale*, 2018, DOI: 10.1039/C7NR08366A.

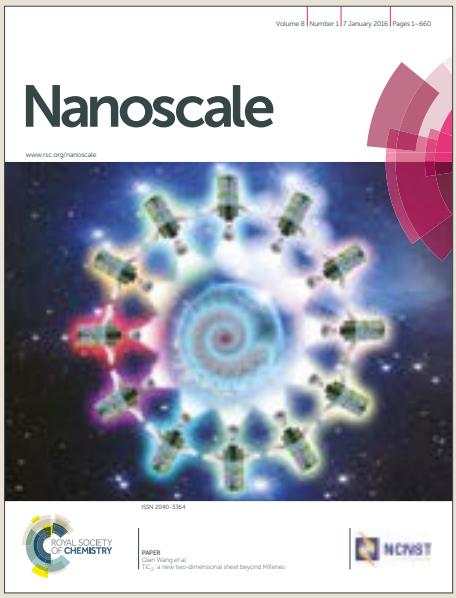

ROYAL SOCIETY OF CHEMISTRY

rsc.li/nanoscale

View Article Online
DOI: 10.1039/C7NR08366A

Journal Name

ARTICLE

Rational Design of 3D Inverse Opals Heterogeneous Composites Microspheres as Excellent Visible-Light-Induced NO_2 Sensor at Room Temperature

Received 00th January 20xx,
Accepted 00th January 20xx

DOI: 10.1039/x0xx00000x

www.rsc.org/

Tianshuang Wang, Qi Yu, Sufang Zhang, Xueying Kou, Peng Sun* and Geyu Lu*

Lower gas sensitivity, the humidity dependence of the gas sensing properties, and long recovery time severely limit the application of room-temperature gas sensor. Herein, to solve these issues, a series of 3D inverse opals (IO) In_2O_3-ZnO heterogeneous composites microspheres (HCMs) are fabricated by ultrasonic spray pyrolysis (USP) employing self-assembly sulfonated polystyrene (S-PS) spheres as sacrificial template. The 3D IO In_2O_3-ZnO HCMs possess highly ordered 3D inverse opals structure and bimodal (meso-scale and macro-scale) pores, which can provide large accessible surface area and rapid mass transfer, resulting in enhanced gas sensing characteristics. Furthermore, the 3D IO architecture and n-n heterojunction can extend the photo absorbing range to visible light area, effectively prolong lifetime of photo-generated charge carriers, and increase separation of visible light generated charges. As a result, the as-prepared 3D IO In_2O_3-ZnO HCMs deliver excellent NO_2 sensing performance under visible light irradiation at room temperature, such as high sensitivity (R_{gas}/R_{air} = 54.3 to 5 ppm NO_2), low detection limit (250 ppb), fast recovery time (188 s), excellent selectivity and humidity independent. The advance in photo-electronic gas sensing properties is attributed to the combining of highly ordered 3D IO microspheres and In_2O_3-ZnO heterogeneous composites.

1. Introduction

Traditional semiconducting metal oxides (SMOs) gas sensors usually operate at elevated temperatures (150-400 °C). However, the high operating temperature will bring power consumption and long term drift problems into gas sensors, because of thermally induced growth of metal oxide nanoparticles. Besides, higher operating temperature may cause an unexpected explosion when detecting flammable and explosive gases.[1] Thus, the development of ultra-high performance room-temperature gas sensors at low fabrication costs has been the focus of research in recent years.

SMOs nanoparticles can be a promising candidate for room-temperature sensing layers, due to their distinctive features such as smaller size and high activity.[2,3] However, most nanoparticles tend to form large and dense secondary agglomerates, which will lead to a decrease in sensitive utilization and largely hamper the employment of nanoparticles as sensing material. As a special kind of microstructure, 3D inverse opals structure could avoid the aggregation between the nanoparticles and exhibit higher gas response at low operating temperature.[4,5] Such special structure will be beneficial for facilitating gas diffusion, and improving the penetration depth of target gas into sensing materials (utility factor), because of the controllable pore size, well-ordered porous architecture and high gas accessibility.[6,7] Besides, the 3D IO structure also could improve the transfer of charge carriers, retard the electron-hole recombination as well as expand the light responding range,[8,9] because of its fully connected skeleton and controlled porous structure.[10,11] Consequently, diverse efforts have been reported to be deployed on designing 3D IO structures.[5-7,12,13] Nevertheless, it is noteworthy that the recently related researches about 3D IO structure are commonly in the form of film fabricated through gravitational sedimentation or spin-coating technique. Thus, the development of a simple and efficient sacrificial templates method facilitating the fabrication of SMOs with 3D IO structure is highly desired.

In order to address the above problem, we report the design and fabrication of microspheres with 3D IO structure by combining USP method and self-assembly sulfonated polystyrene (S-PS) spheres template routes. Compared with traditional method, the one-step spray pyrolysis of droplets containing metallic source and macro-scale S-PS spheres was developed as a feasible synthetic route for the preparation of 3D IO structure in SMOs microspheres. On top of microstructure optimization, the fabrication of heterogeneous composites

[a] State Key Laboratory on Integrated Optoelectronics, College of Electronic Science and Engineering, Jilin University, 2699 Qianjin Street, Changchun 130012, People's Republic of China. E-mail: pengsun@jlu.edu.cn

Electronic Supplementary Information (ESI) available. See DOI: 10.1039/x0xx00000x

View Article Online
DOI: 10.1039/C7NR08366A

materials could lead to further improvement of gas sensing characteristics due to the synergic effects at the interfaces. Therefore, much studies were reported on the synthesis and gas sensing applications of heterogeneous composites.[14-17] Heterogeneous composites materials can increase adsorption capability by injecting more electrons into the active surface area, assist the charge separation process of the electron-hole pairs before they recombining, as well as modulate potential barriers at the grain boundaries.[18] However, in all the aforementioned studies, the actual operating temperatures of most gas sensors are higher than 100 °C. Even though the operating temperatures of some sensors are below 60 °C, they could not completely recover at their optimal operating temperature. Apart from regulating the morphology of SMOs and designing heterogeneous composites materials, the surface light irradiation technique is regarded as an effective strategy to improve gas sensing properties and really decrease operating temperature to room temperature since Camagni demonstrated that ultraviolet (UV) illumination can significant enhance oxide sensor performance.[19] In recent years, there have been many reports on gas sensors based on UV light activated oxide semiconductors.[20-23] However, the research on the improvement of gas sensing properties via visible light illumination is seldom reported.[24-26] Therefore, for the purpose of benefiting from the advantages of both the 3D IO microspheres structure and heterogeneous composites system, we have fabricated 3D IO In_2O_3-ZnO HCMs and used the narrow band gap semiconductor In_2O_3 as an ideal photo-sensitizer, leading to visible-light-driven materials with enhanced photo-electronic gas sensing characteristics. To the best of our knowledge, there is currently no literature focus on the fabrication of 3D IO In_2O_3-ZnO HCMs via USP method and as a high performance room-temperature NO_2 sensor under visible light irradiation.

In this investigation, we present a feasible and versatile synthetic method (USP) to fabricate 3D IO In_2O_3-ZnO HCMs employing self-assembly S-PS spheres as a sacrificial template. Such architecture gave a promising structural platform for the fabrication of photo-electronic gas sensor due to its highly ordered inverse opals structure for accelerating gas diffusion and improving light utilization. Based on this, the 3D IO In_2O_3-ZnO HCMs as an ideal photo-induced sensing material for room-temperature gas sensor was demonstrated by their ultra-high performance toward low concentrations of NO_2 under visible light irradiation. Furthermore, the effect of humidity on the photo-electronic gas sensing properties of the NO_2 sensor based on 3D IO In_2O_3-ZnO HCMs before or after visible light illumination at room temperature was also investigated. The gas sensing mechanism of the 3D In_2O_3-ZnO HCMs under visible light irradiation is proposed and discussed. The main focuses of this research are on the development of 3D inverse opals heterogeneous composites microspheres via one-step synthesis method and demonstration of their potential use as excellent visible-light-driven NO_2 sensor with better moisture resistance at room temperature.

2. Experimental procedures

2.1 Preparation of precursor materials

Polystyrene (PS) spheres were fabricated by emulsion-free polymerization method,[27] and surface-modified with H_2SO_4 (40ml, 95%) at 40 °C for 6h. The sulfonated process could produce sulfonic acid ($SO_3^-H^+$) groups as PS spheres' hydrophilic shells, which were able to form complexes with a large amount of metal ions.[28] The obtained product was washed for four times using distilled water and ethanol, respectively. Finally, dried at 60 °C for 1 day.

2.2 Preparation of gas sensing materials

3D IO In_2O_3-ZnO HCMs were prepared by the USP method. The ultrasonic spray solution for the 3D IO In_2O_3-ZnO HCMs were prepared by adding various amounts of $In(NO)_3$ and $Zn(NO)_2$ into the mixed solution containing 15 ml of distilled water, 300 μl of hydrogen peroxide solution (30%, H_2O_2), an appropriate volume of hydrochloric acid solution (38%, HCl), and well-dispersion surface-modified S-PS spheres. And the mixtures were stirred for 4 h at room temperature. The Zn/In mole ratios in the precursor solutions were set as 0:1 (pure In_2O_3), 1:3, 1:1, 3:1 and 1:0 (pure ZnO), which were marked as S1, S2, S3, S4 and S5 respectively for convenience. The spray solution for the Solid In_2O_3-ZnO HCMs (the Zn/In mole ratios in the precursor solutions were set as 1:1) was prepared without the S-PS spheres, which was marked as S6 for convenience. The droplets of the spray solutions were produced by an ultrasonic transducers (resonant frequency = 1.7 MHz), and the mists were subsequently transported to a tubular reactor (Temperature: 700 °C) by flowing N_2 gas (flow rate = 500 sccm). The obtained precursor powder was collected from the water-filled conical flask, and washed with deionized water and ethanol for several times. After dried at 80 °C for 10 h, the powder was transferred to the muffle furnace and annealed at 600 °C for 3 h with a temperature rate of 10 °C min^{-1} to completely remove the template.

2.3 Materials characterization

Crystal phase was analyzed by X-ray diffraction analysis (XRD; Rigaku D/Max 2550) using Cu Kα radiation (λ = 0.154 nm). The detail microstructure was observed by field-emission scanning electron microscopy (FESEM; JEOL JSM-7500F), transmission electron microscopy (TEM; JEOL JSM-2100F) and high-resolution transmission electron microscopy (HRTEM; JEOL JSM-2100F). X-ray spectrometry (EDS) pattern were also observed through the attachment of TEM. The specific surface area and pore-size distribution were measured by Brunauer-Emmet-Teller (BET) and Barrett-Joyner-Halenda (BJH) methods using N_2 adsorption-desorption isotherms (Micrometrics Gemini VII). XPS measurement was carried out by ESCALAB 250 X-ray photoelectron spectrometer using X-ray source (Al Kα hv = 1486.6 eV). The photoluminescence (PL) spectrum and the absorption spectra were recorded by RF-5301PC (Shimadzu, Japan) fluorescence spectrophotometer and UV-2550 (Shimadzu, Japan) spectrophotometer, respectively.

2.4 Fabrication and measurement of the gas sensor

View Article Online
DOI: 10.1039/C7NR08366A

The gas sensor instrument is illustrated in **Figure S1**. The fabrication process was described as follows: First, the homogeneous paste was obtained by mixing a certain amount of the powders with an appropriate amount of isopropanol in a weight ratio of 5:1. Secondly, the paste was coated on an alumina tube to form a thick sensing film. Finally, the device was calcined at 250 °C for 1 h. A static testing system (22 ± 2 RH%) was used to investigate the gas sensing properties.[14] The visible light source was light emitting diode. The response was defined as R_{air}/R_{gas} (Reducing gas, such as C_2H_5OH, C_6H_6, etc.) or R_{gas}/R_{air} (Oxidizing gas, such as NO_2, O_3, etc.). Sensing speed (response time (τ_{res}) and recovery time (τ_{rec})) was measured according to the change in resistance value.

3. Results and discussion

The XRD pattern of the as-prepared S1-S5 samples was shown in **Figure S2**. As can be seen that the as-prepared 3D IO In_2O_3-ZnO HCMs (S2-S4 samples) were mixtures of hexagonal ZnO and cubic In_2O_3 crystallites, the hexagonal ZnO (JCPDS card 36-1451) gradually appeared with the increase of ZnO content. The XRD pattern of the S1 sample could be well indexed to body-centered cubic phase In_2O_3 (JCPDS card 06-0416). And the XRD pattern taken from the S5 sample (3D IO ZnO microspheres) could be indexed to hexagonal phase (JCPDS card 36-1451) for ZnO. Besides, the XRD pattern of S6 sample was similar with that of S3 sample (**Figure S3**).

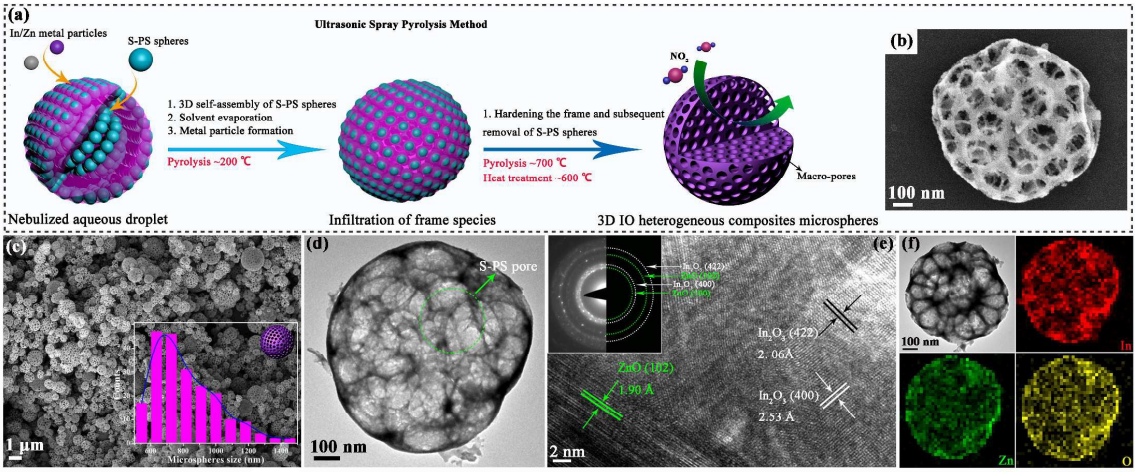

Figure 1. (a) Illustration of the process flow to fabricate 3D IO In_2O_3-ZnO HCMs; (b) Typical SEM image of the as-prepared product 3D IO In_2O_3-ZnO HCMs (S3 sample); (c) SEM image and corresponding size distribution histogram of S3 sample; (d) TEM image of individual S3 sample; (e) HRTEM image and SAED pattern of S3 sample; (f) TEM image of an individual S3 sample and its EDS element mapping images of In, Zn and O, respectively.

For the synthesis of of 3D IO HCMs, we combined USP method with self-assembly templating routes. The diameter of most S-PS spheres was between 80 and 120 nm (**Figure S4**). As shown in **Figure 1**(a). The solution mixed with S-PS spheres consolidation was nebulized by ultrasonic spray, and then the resulting aqueous droplets were carried into the furnace through an inert gas stream, the aqueous droplets would go through two processes: (i) 3D self-assembly of S-PS spheres, solvent evaporated and metal particle formation (pyrolysis ~200 °C); (ii) hardening the frame and subsequent removal of S-PS spheres (pyrolysis ~700 °C and heat treatment ~600 °C), resulting the formation of macro-scale pores (approximately 80 nm) and meso-scale pores (approximately 4 nm).[27,29] So as to improve specific surface area of heterogeneous composites. The microstructure of the as-prepared special 3D IO In_2O_3-ZnO HCMs (S3 sample) was presented in Figure 1(b). As can be clearly seen, S3 sample exhibited a 3D spherical framework with sufficient interconnected, and the diameter of pores was smaller than the removed S-PS spheres, probably due to the shrinkage of spheres diameters during calcination.[30] Typical SEM images of the other samples (S1, S2, S4 and S5) also showed 3D ordered IO skeletons (**Figure S5**(a-d)). SEM image (Figure 1(c)) showed that the morphology of S3 sample was isolated uniform 3D IO microspheres. And a histogram analyzed the size distribution of two hundreds of S3 sample (the inset image of Figure 1(c)), which exhibited a narrow size distribution with the microspheres diameter ranging between 545 and 1455 nm, with an average diameter of 727 nm.

Detailed information about the morphology of the as-synthesized S3 sample was further obtained by transmission electron microscopy (TEM) analysis, image of which was shown in Figure 1(d). All spherical pores were well developed inside the microspheres and continuously connected each other. Such architecture indicated that the shape of S-PS spheres remained uniformly and the oxide walls were formed stably among these pores, even after burning of the S-PS templates and decomposition of the precursors. The TEM images of 3D IO In_2O_3 and ZnO microspheres (S1 and S5 samples) exhibited that the microstructure of S1 and S5 samples were similar with the S3 sample (**Figure S6**(a) and (d)). It could be concluded that the introduction of different components of SMOs did not affect the morphology of 3D IO HCMs. The lattice distances in Figure 1(e) were calculated to be about

View Article Online
DOI: 10.1039/C7NR08366A

2.06 Å and 2.53 Å, which could be assigned to the (422) and (400) plane of the cubic phase In_2O_3. Also, as shown in Figure 1(e), the (102) plane of the wurtzite hexagonal phase ZnO corresponding to the interplanar spacing of 1.90 Å. In addition, the lattice planes of ZnO (102), In_2O_3 (422) and In_2O_3 (400) were identified in the SAED pattern of S3 sample (the inset image of Figure 1(e)), which were partially observed as well in the HRTEM images. Crystallographic structures of S1 and S5 samples were observed, with crystal planes of In_2O_3 (422), In_2O_3 (332), ZnO (102), and ZnO (103) by Figures S6(b) and (e), respectively. Figure S6(c) and (f) were the corresponding selected-area electron diffraction (SAED) patterns, showing a set of polycrystal electron diffraction rings corresponding to the cubic phase In_2O_3 and wurtzite hexagonal phase ZnO, respectively. We carried out the EDS analysis (Figure 1(f)) to confirm the distribution of corresponding elemental spacial of the individual S3 sample.

Nitrogen physisorption experiments were performed on the S3 and S6 samples. The N_2 adsorption/desorption isotherms were shown in **Figure 2**(a), the S3 sample exhibited a shape that was between type II and type IV isotherm with H3 hysteresis loops, reflecting the characteristic of meso-porous structure. In contrast, the S6 sample exhibited type II isotherm that was the typical characteristic of non-porous structure. Consequently, the specific surface area of the inverse opals structure sample was determined to be about 32.7 m^2g^{-1} (Figure 2(b)), which was substantially larger than that of the solid structure sample (Figure 2(c)). From these observations, we could conclude that both the inner and outer surfaces of 3D IO In_2O_3-ZnO HCMs were exposed to the gas phase. Furthermore, the inverse opals microspheres had both meso-pore (4 nm) and macro-pore (80 nm) structures (Figure 2(d)). Among them, the generation of meso-scale pore was attributed the decomposition of S-PS spheres template.[30] However, no obvious pores were found in the solid microspheres (Figure 2(e)). Thus, we could deduce that this novel structure (3D IO microspheres) will obviously improve gas sensing properties compared with solid microspheres.

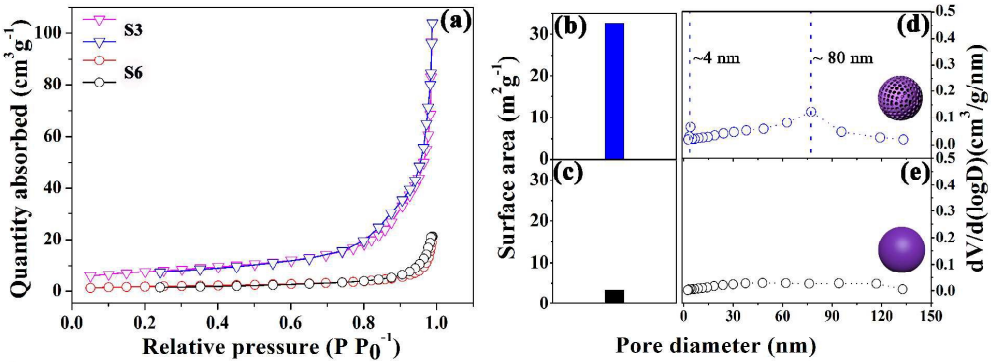

Figure 2. (a) N_2 adsorption/desorption isotherms of S3 and S6 samples. (b-e) BET surface areas and pore-size distributions of (b, d) S3 and (c, e) S6.

The UV-vis absorption tests of the as-prepared S1-S5 samples were displayed in **Figure 3**(a). The 3D IO ZnO microspheres (S5) showed a clear absorption edge at about 390 nm, and the absorption edge of the 3D IO In_2O_3 microspheres (S1) moved to the visible-light region (480 nm). However, by comparison with S1 and S5, 3D IO In_2O_3-ZnO HCMs (S2-S4 samples) exhibited much stronger absorption in the visible light region of 400-700 nm and the absorption edge had an obvious red shift to about 550 nm. These results can be attributed to the formation of In_2O_3-ZnO heterojunction.[24] In addition, according to the UV-vis absorption spectra of the S1-S5 samples, the band gap energies of these samples can be calculated from the Tauc plot equation (**Figure S7**(a-f)).[31] The band gap energies of heterogeneous composites (S2-S4 samples) tended to be smaller values, compared to S1 (pure In_2O_3 ~ 2.92 eV) and S5 (pure ZnO ~ 3.22 eV) samples.[32,33] The trend changes in the test results were similar to those previously reported in the literature.[22] Besides, the S3 sample possessed the lowest band gap energy (Figure S7(d)), thus leading to more excited photo-generated charges under the same illumination conditions.[26] All these data distinctly demonstrated that the combination of In_2O_3 with ZnO to produce a heterogeneous composites with an intimate heterojunction could lead to the red-shift of optical absorption and form an effective absorption for visible light.

For the purpose of demonstrating the formation of heterojunction could be helpful for hindering the recombination of photo-generated charge carriers, the photoluminescence (PL) spectrum tests of S1-S5 samples were also carried out. PL spectrum was utilized to investigate the transfer and recombination behavior of the excited electrons and holes in materials. As shown in Figure 3(b), PL spectra of S1-S5 samples were all exhibited two prominent peaks centered at around 389 and 468 nm in the visible light region. One peak at ~389 nm (UV luminescence) could be assigned to near band edge emission, and the other peak at ~468 nm (Blue luminescence) was attributed to the radioactive recombination of a photo-generated hole with an electron occupying the oxygen vacancy. Above results were similar with the PL emission mechanism of ZnO and SnO_2 semiconductors.[34-37] The PL emission intensity of S2-S4 samples decreased obviously, indicating that the recombination of photo-generated charge carriers was inhibited greatly in the 3D IO In_2O_3-ZnO HCMs. And the overall PL emission intensity of S3 sample was the lowest, showing its lowest recombination rate of electron-hole pairs. In composites, ZnO enhanced charge carriers mobility and decreased the recombination rate of active charge carriers, and In_2O_3 acted as an active light absorption center. Therefore, the formation of heterogeneous composites is the key factor in realizing visible-light-driven photo-electric gas sensing.

Furthermore, in order to prove that the novel microstructure (3D IO microspheres) was also beneficial for hindering the recombination of the photo-generated charge carriers, thereby enhancing the photo-electronic gas sensing properties under visible light

View Article Online
DOI: 10.1039/C7NR08366A

irradiation at room temperature. UV-vis absorption and PL spectrum were carried out on the In_2O_3-ZnO HCMs with highly ordered 3D IO structure and solid construction (S3 and S6 samples). The UV-vis absorption spectrum was measured within the wavelength range of 200-800 nm, it was evident that the highly ordered 3D IO structure generated a red shift in the absorption edge (Figure 3(c)), leading to efficient utilization of visible light.[8] Compared with the S6 sample, the overall PL emission intensity of S3 sample was the lowest, reflecting that the introducing of highly ordered 3D IO structure in In_2O_3-ZnO HCMs may decrease the recombination rate of electron-hole pairs (Figure 3(d)). The highly ordered 3D IO structure could efficiently improve the utilization of visible light and lead to effective separation of visible-light-generated charges, thus being favourable for improving photo-electronic gas sensing properties.

For further investigating the elemental composition, the oxidation states and the chemical environment of In and Zn elements in the S1-S5 samples, XPS analysis were performed in **Figure S8**.

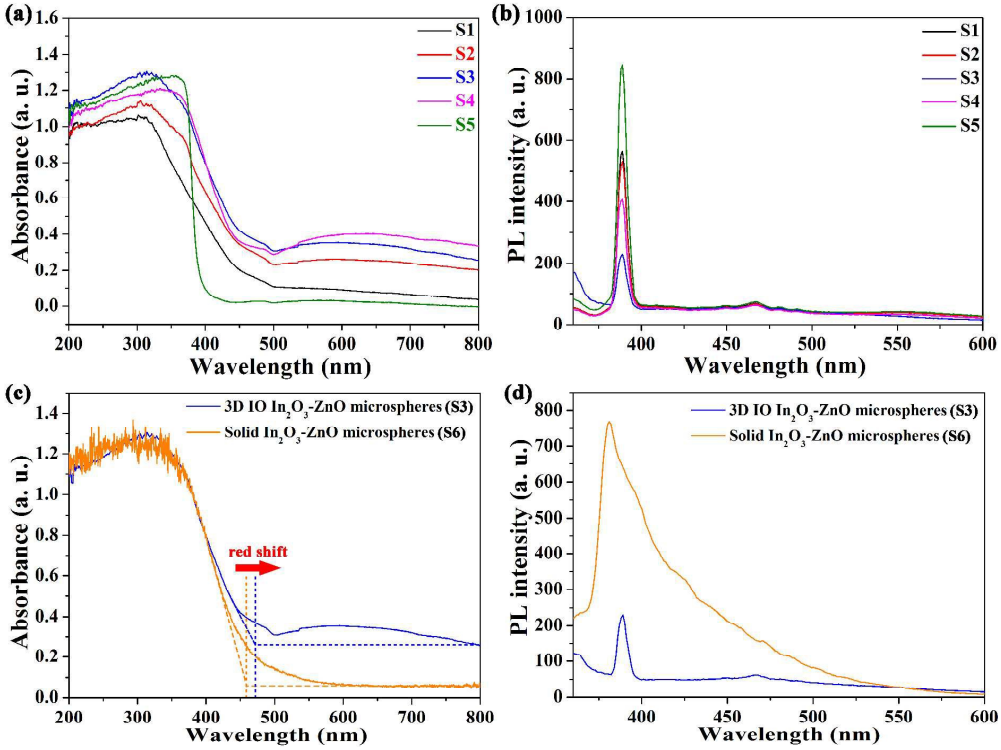

Figure 3. (a) UV-vis absorption spectra and (b) Photoluminescence (PL) spectra of 3D IO In_2O_3-ZnO HCMs with different component ratios (S1-S5 samples); (c) UV-vis absorption spectrum and (d) Photoluminescence (PL) spectrum of 3D IO In_2O_3-ZnO HCMs (S3 sample) and Solid In_2O_3-ZnO HCMs (S6 sample), the PL spectra were recorded at room temperature at excitation wavelength of 340 nm.

4. Photo-electronic gas sensing characterization

Photo-electronic gas sensors were fabricated from the as-prepared S1-S6 samples, and their gas sensing performances were tested under visible light irradiation at room temperature. **Figure S9**(a) exhibits the gas responses of the S1, S3 and S5 sensors toward 5 ppm NO_2 before and after visible light illumination. It was found that after visible light illumination, 4.2-fold and 6.3-fold enhanced NO_2 response (R_{gas}/R_{air} = 54.3 at 5 ppm) were observed with 3D IO In_2O_3-ZnO HCMs (S3) when compared with that of (S1) 3D IO In_2O_3 microspheres (R_{gas}/R_{air} = 13 at 5 ppm) and (S5) 3D IO ZnO microspheres (R_{gas}/R_{air} = 8.64 at 5 ppm), respectively. In addition, the gas responses of these sensors under visible light irradiation were drastically increased. In order to find an optimized atom ratio of Zn/In, we carried out NO_2 sensing test with different mole ratios of Zn/In (1:3, 1:1 and 3:1) (Figure S9(b)). Among these sensors, the S3 sensor showed the highest response to 5 ppm NO_2, as well as fast response and recovery speeds. In addition, in order to further demonstrate that the highly ordered 3D IO structure was helpful for improving the room-temperature gas sensitivity under visible light irradiation, the room-temperature gas sensing transients of S3 and S6 samples under visible light irradiation were shown in Figure S9(c). The gas response of S3 toward 5 ppm NO_2 was higher than that of S6, which is consist with the phenomenon optical characteristics. The dependence of the room-temperature gas responses on the NO_2 concentration for the S1, S3, and S5 sensors under visible light irradiation was exhibited in Figure S9(d). The gas responses of these sensors displayed good linearity with the increase of NO_2 concentrations (0.25-5 ppm), and the detection limit of the S3 sensor was 250 ppb with high response of 4.7. Confirming that the S3 sensor is a promising candidate for the detection of low concentration of NO_2. Gas selectivity is one of the most important parameters of sensors in practical applications. The selectivity of the S3 sensor was exhibited in Figure S9(e), it could be found that a excellent NO_2 selective characteristic under visible light irradiation was obtained with negligible cross responses

View Article Online
DOI: 10.1039/C7NR08366A

(R_{air}/R_{gas} or $R_{gas}/_{air}$ < 5) to interfering analytes such as toluene, CO, ethanol, ammonia, and O_3 et al. The above results suggested that the introducing of highly ordered 3D IO structure, the formation of heterojunction and the introducing of visible-light-excitation were effective methods for improving the NO_2 gas sensitivity at room temperature.

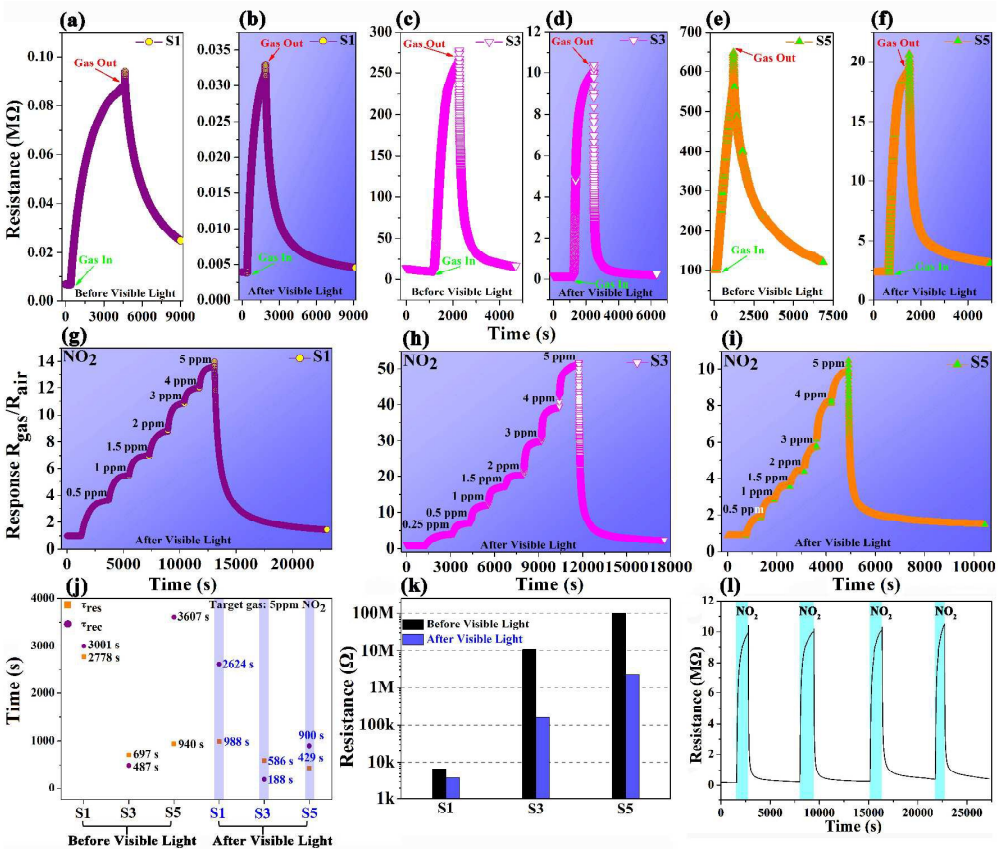

Figure 4. (a-f) Gas sensing transients of the S1, S3 and S5 sensors when exposed to 5 ppm NO_2 before and after visible light and (j) their corresponding τ_{res} and τ_{rec} plots. (g-i) Dynamic gas sensing transients of the S1, S3 and S5 sensors to different concentration range of NO_2 after visible light at room temperature. (k) Resistances of the S1, S3 and S5 sensors in air before and after visible light as a function of composition. (l) The repeatability of the S3 sensor response at cyclic exposure to 5 ppm NO_2 under visible light irradiation at room temperature.

The dynamic resistance transition characteristic of these three sensors (S1, S3 and S5) exposure to 5 ppm of NO_2 before and after visible light irradiation were shown in **Figure 4**(a-f). The resistances of all sensors increased when exposed to a oxidizing gas (NO_2), reflecting the typical characteristic of n-type sensing materials. The gas response of S3 sensor under visible light irradiation were higher than that of S1 and S3 sensors, which was attributed to the enhanced separation of visible-light-generated electrons and holes in the In_2O_3-ZnO heterogeneous composites. The measurements results verified the speculation based on the PL emission spectra characterization results. The resistance change with time under different NO_2 gas concentrations was shown in Figure 4(g-i). At room temperature, the S3 sensor showed very stable response characteristics down to 250 ppb of NO_2 and could rapidly return to initial resistance when exposed to air. The S1 and S5 sensors also exhibited stable response characteristics, but the gas responses of these two sensors were lower than the S3 sensor and their detection limits were all 500 ppb. The resistances of S1, S3 and S5 sensors under visible light irradiation were much lower than those of these three sensors in the dark (Figure 4(k)). Resistance of pure In_2O_3 was much lower than that of pure ZnO. Generally, in a dark atmosphere, the resistance of In_2O_3-ZnO composites was higher than that of pure In_2O_3 due to the formation of a n-n junction. However, the resistance of pure ZnO was higher than that of In_2O_3-ZnO, which may ascribed to the presence of In^{3+} in ZnO structures results in the increases of electrons concentration. As follows:

$$2ZnO \xrightarrow{In_2O_3} 2In_{Zn}^{\bullet} + 2e^{'} + 2O_O^x + \frac{1}{2}O_2(gas) \qquad (1)$$

According to equation (1), the substitution of In^{3+} at the site of Zn^{2+} can be compensated by the electronic compensation mechanism, the oxygen molecules are generated by the incorporation reaction.[38] Based on Figure 4(a-f), the corresponding τ_{res} and τ_{rec} of the S1, S3 and S5 sensors before and after visible light illumination were calculated and depicted in Figure 4(j). The results demonstrated that visible light could accelerate the response and recovery speeds of sensors. Especially, the τ_{res} of the S3 sensor to 5 ppm NO_2 was reduced from 697 s

View Article Online
DOI: 10.1039/C7NR08366A
Journal Name ARTICLE

(without visible light irradiation) to 586 s (under visible light irradiation), and the τ_{rec} was shortened from 487 s to 188 s. Moreover, under visible light irradiation condition, τ_{res} and τ_{rec} of 3D IO In_2O_3-ZnO HCMs (S3) were much lower than those of 3D IO In_2O_3 (S1) and ZnO (S5) microspheres. As shown in Figure 4(l), the S3 sensor exhibited good response repeatability and recyclability to NO_2. Furthermore, the long-term stability of the gas sensor was displayed in **Figure S10**, the 3D IO In_2O_3-ZnO HCMs (S3) remained highly stable response toward 5 ppm NO_2 under visible light irradiation at room temperature for 30 days. **Table S1** compared our room-temperature NO_2 sensor with other results reported in literature based on SMOs at room temperature. The results confirmed that the gas sensor based on the 3D IO In_2O_3-ZnO HCMs (S3) had a higher response and shorter recovery time at room temperature under visible light irradiation.

The effect of humidity on the photo-electronic gas sensing properties of the S3 sensor to 5 ppm NO_2 before or after visible light illumination at room temperature was investigated. As shown in **Figure 5**(a-d), without visible light irradiation, the gas response of the S3 sensor significantly decreased in humid atmosphere and the R_a value also decreased obviously with increasing humidity (**Figure S11**(a)). Moreover, it was noteworthy that the humidity significantly increase the recovery time (Supplementary Figure S11(b)). Generally, when an n-type oxide semiconductor lies in humid atmosphere, the water vapor will react with the adsorbed oxygen species and release electrons to the semiconductor, meantime, the active site on the material surface is covered gradually by water vapor.[39,40] Therefore, the introduction of water vapor generally decreases the sensor resistance and the gas response.

Under visible light irradiation, the adsorbed water vapor on the surface of 3D IO In_2O_3-ZnO HCMs can be decomposed by the photo-generated charges, as shown by the following equation.[41]

$$\mathrm{H_2}O(vapor) + h^+(hv) \rightarrow \frac{1}{2}O_2(gas) + 2H^+ + 2e^-(hv) \quad (1)$$

$$2\mathrm{H}^+ + 2e^-(hv) \rightarrow H_2(gas) \quad (2)$$

Overall reaction

$$\mathrm{H_2}O(vapor) + h^+(hv) + 2e^-(hv) \rightarrow H_2(gas) + \frac{1}{2}O_2(gas) \quad (3)$$

Thus, it will increase the humidity independence of the gas sensing characteristics steadily by the introduction of visible light. In humid atmosphere (r.h. = 50% and 80%), the S3 sensor showed very stable response characteristics to 5 ppm NO_2 and could rapidly return to initial resistance when exposed to air (Figure 5(e-g)). The sensor showed little fluctuation of response to 5 ppm NO_2 with increasing humidity (Figure 5(h)). In addition, the response and recovery times of the S3 sensor did not change significantly as humidity increased (Supplementary Figure S11(b)). The adsorbed water vapor can be effectively decomposed by the overall reaction (reaction (3)) because the electron and hole were continuously generated under visible light irradiation. As shown in Figure S11(a), the R_a increased a little under visible light irradiation with the increasing of the relative humidity. According to the overall reaction (reaction (3)), we could speculate that the decomposition of water vapor on the material surface was accomplished via capturing more photo-generated electrons from the conduction band, which led to a little increase in resistance (R_a). From the above descriptions, it can be concluded that the humidity independent gas sensors are achieved by the introduction of visible light. The interaction of the photo-generated charges with water vapor results in photo-decomposition of water vapor.

View Article Online
DOI: 10.1039/C7NR08366A

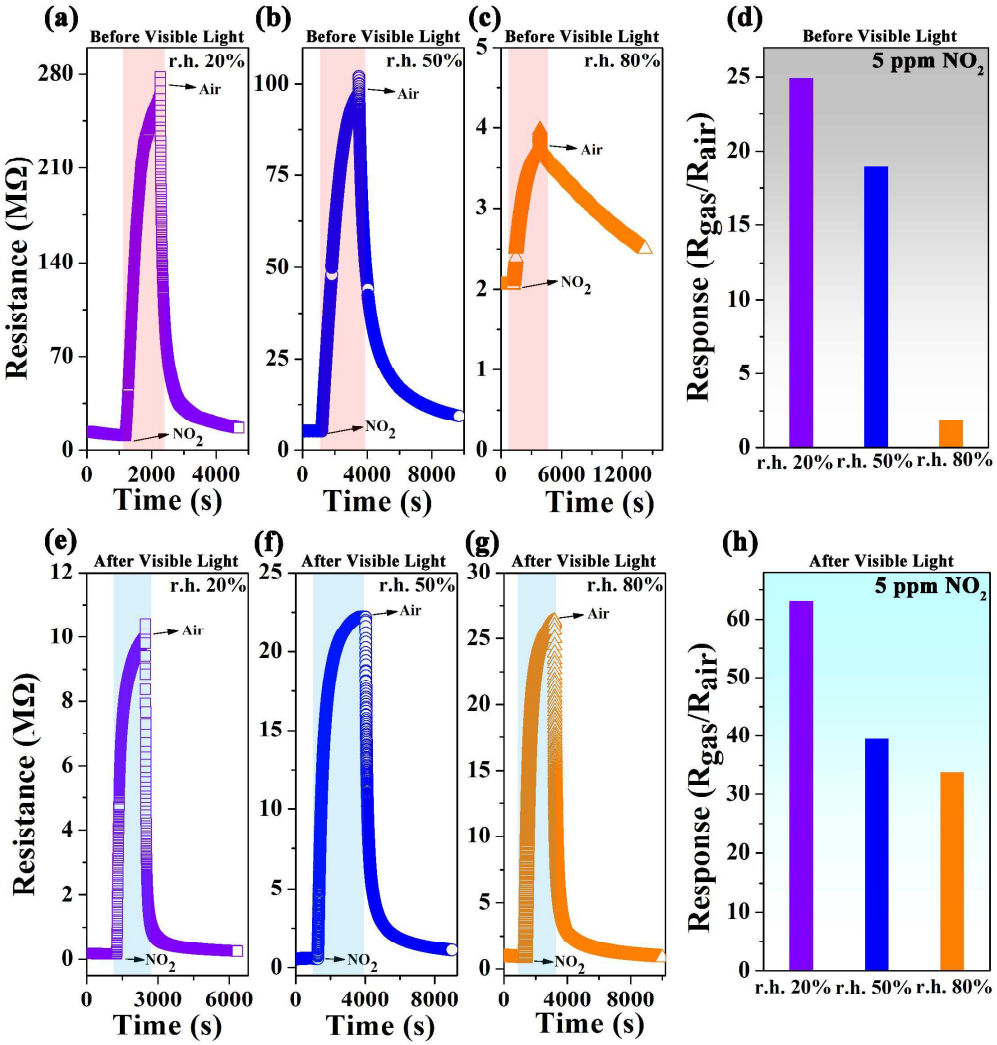

Figure 5. Dynamic gas sensing transients and gas responses of the S3 sensor toward 5 ppm NO_2 with various relative humidity (r.h. = 20%, 50% and 80%) at room temperature (a-d) before visible light and (e-h) after visible light.

The mechanism responsible for the improved NO_2 sensing performance of the 3D IO In_2O_3-ZnO HCMs under visible light irradiation was investigated. The band edge positions of ZnO and In_2O_3 were calculated by the Mulliken electronegativity method.[42,43] As schematically shown in Figure 6(a), when In_2O_3 was in contact with ZnO, noticeable electron will transfer from In_2O_3 to ZnO, and leading to the surface energy bands bending in both In_2O_3 (band gap = 2.92 eV) and ZnO (band gap = 3.22 eV) due to the formation of In_2O_3-ZnO heterojunction.[38] When the 3D IO In_2O_3-ZnO HCMs were illuminated by visible light, only In_2O_3 can be excited to generate electron-hole pairs because of its narrow energy band.[32] Many visible-light-generated electrons transferred from the conduction band of In_2O_3 to the conduction band of ZnO and remained on the surface of the semiconductor material, leading to a high density of electrons in the conduction band of ZnO. Upon exposure to the air, the visible-light-generated electrons were usually trapped by oxygen (O_2) to produce molecular species (O_2^-) at room temperature. Besides, the interaction of the photo-induced holes with oxygen ions, which results in photo-desorption of oxygen species.[22] Therefore, based on above analysis, the resistance of the sensor reduced after visible light illumination. The reactions that occurred on the surface in the presence of air were as follows:

$$O_2(gas) \leftrightarrow O_2(ad) \quad (1)$$

$$O_2(ad) + e^-(hv) \leftrightarrow O_2^-(ad) \quad (2)$$

$$O_2^-(ad) + h^+(hv) \leftrightarrow O_2(gas) \quad (3)$$

The heterojunction between In_2O_3 and ZnO can reduce the rate of charge recombination by separating visible-light-generated electron-hole pairs efficiently, leading to a high density of electrons in the conduction band of ZnO and a remarkable photo-electronic gas sensing properties improvement. During the exposure of the sensor to NO_2 gas, the NO_2 directly adsorbs on the surface through interaction

View Article Online
DOI: 10.1039/C7NR08366A

with the photo-generated electrons, indicating that an abundance of photo-generated electrons on the surface of ZnO will be trapped by NO_2, thus inducing large resistance variation of the 3D IO In_2O_3-ZnO HCMs (Figure 6(b)). The reaction occurs as equation (1).[44]

$$2NO_2(gas) + e^-(hv) \rightarrow 2NO(hv) + O_2^-(hv) \quad (1)$$

In addition, under continuous visible light irradiation, when the sensor was transferred to the air, the photons contributed to the desorption of the photo-induced NO (hv) and O_2^- (hv) from the surface of the material. Therefore, in In_2O_3-ZnO hybrid heterogeneous composites, the visible light is helpful to shorten response and recovery time.[21]

It is well known that the microstructure of sensing materials is also an important factor for affecting gas sensing performance. Compared with the solid microspheres, 3D IO microspheres possess larger surface area, porous structure and interconnected channels that can significantly enhance gas accessibility of the entire sensing layers, leading to the enhancement in sensing performances (Figure 6(c)). Moreover, the results of UV-vis absorption spectra and PL spectra have demonstrated that the highly ordered 3D IO structure can improve the utilization of visible light and hinder the recombination of the photo-generated charge carriers. This means that the amount of oxygen that can be absorbed and ionized is maximized. This is another reason why the 3D IO microspheres show excellent gas sensing properties.

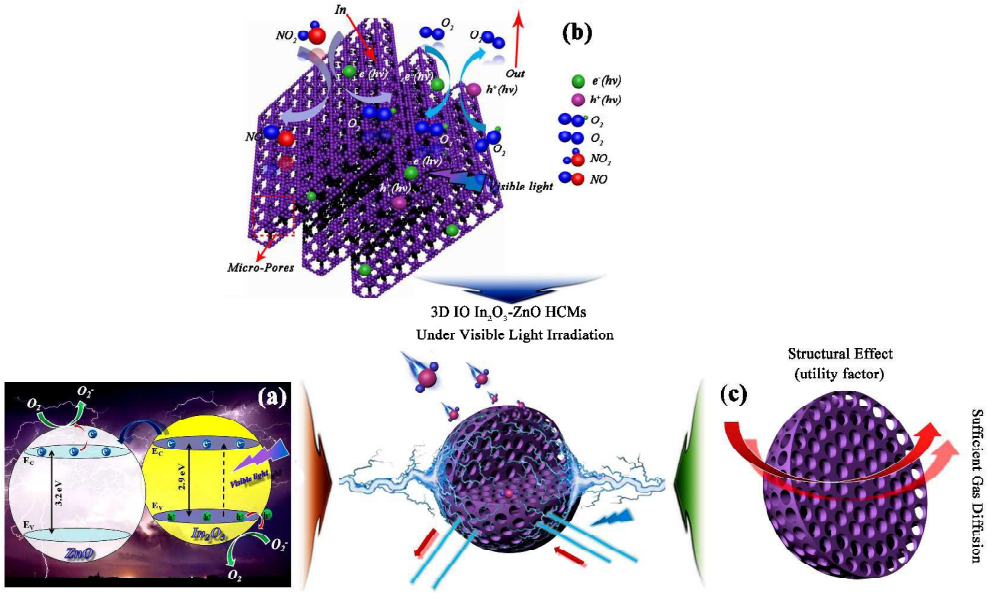

Figure 6. (a) Sketch of conduction and valence band levels in ZnO and In_2O_3. (b) Schematic illustration of NO_2 sensing mechanism of 3D IO In_2O_3-ZnO HCMs under visible light irradiation. (c) 3D IO ordered structure improved gas diffusion and gas transport.

5.Conclusion

In summary, self-assembly sulfonated PS spheres were employed to as a sacrificial template, then the 3D IO In_2O_3-ZnO HCMs were prepared via USP. Photo-electronic gas sensing characterizations under visible light irradiation at room temperature showed that the sensor based on 3D IO In_2O_3-ZnO HCMs with a [Zn]:[In] ratio of 1:1 could detect NO_2 with outstanding selectivity, low detection limit, as well as fast response time and recovery time. In addition, the 3D IO In_2O_3-ZnO HCMs sensor exhibited the humidity independent room-temperature NO_2 sensing performance under visible light irradiation. Such performance improvement was accomplished by the formation of n-n heterojunction structure, the introducing of highly ordered 3D IO structure and the increased electrons induced by visible light. This work provides a straightforward and general synthetic route for preparing the 3D IO heterogeneous composites microspheres to explore new room temperature gas sensor with high performance.

Conflicts of interest

There are no conflicts to declare.

Corresponding author

E-mail: pengsun@jlu.edu.cn
E-mail: lugy@jlu.edu.cn

View Article Online
DOI: 10.1039/C7NR08366A

ORCID

Peng Sun: 0000-0002-9509-9431

Acknowledges

This work is supported by the National Key Research and Development Program of China (No. 2016YFC0207300). National Nature Science Foundation of China (No. 61722305, No. 61503148, No. 61520106003, No. 61327804). National High-Tech Research and Development Program of China (863 Program, No. 2014AA06A505). Science and Technology Development Program of Jilin Province (No. 20170520162JH). China Postdoctoral Science Foundation funded project (No. 2017T100208 and No. 2015M580247). Graduate Innovation Fund of Jilin University (No. 2017173).

References

1. J. Zhang, X. H. Liu, G. Neri and N. Pinna, Nanostructured materials for room-temperature gas sensors, Adv. Mater., **2016**, 28, 795-831.
2. G. Korotcenkov, Metal oxides for solid-state gas sensors: What determines our choice? Mater. Sci. Eng. B **2007**, 139, 1-23.
3. M. E. Franke, J. T. Koplin and U. Simon, Metal and metal oxide nanoparticles in chemiresistors: does the nanoscale matter? Small **2006**, 2(1), 36-50.
4. R. W. J. Scott, S. M. Yang, G. Chabanis, N. Coombs, D. E. Williams and G. A. Ozin, Tin dioxide opals and inverted opals: near-ideal microstructures for gas sensors, Adv. Mater., **2001**, 13, 1468-1472.
5. L. C. Jia, W. P. Cai, H. Q. Wang, F. Q. Sun and Y. Li, Hetero-apertured micro/nanostructured ordered porous array: layer-by layered construction and structure Induced sensing parameter controllability, ACS Nano, **2009**, 3, 2697-2705.
6. R. Q. Xing, L. Xu, Y. S. Zhu, J. Song, W. F. Qin, Q. L. Dai, D. L. Liu and H. W. Song, Three-dimensional ordered SnO_2 inverse opals for superior formaldehyde gas-sensing performance, Sens. Actuators B, **2013**, 188, 235-241.
7. Y. S. Zhu, W. Xu, H. Z. Zhang, W. Wang, S. Xu and H. W. Song, Inhibited long-scale energy transfer in dysprosium doped yttrium vanadate inverse opal, J. Phys. Chem. C, **2012**, 116, 2297-2302.
8. L. C. Chen, L. Z. Xie, M. Z. Wang and X. W. Ge, Preparation of three-dimensional inverse opal SnO_2/graphene composite microspheres and their enhanced photocatalytic activities, J. Mater. Chem. A, **2015**, 3, 2991-2998.
9. T. Toyoda, W. Yindeesuk, T. Okuno, M. Akimoto, K. Kamiyama, S. Hayasecd and Q. Shen, Electronic structures of two types of TiO_2 electrodes: inverse opal and nanoparticulate cases, RSC Adv., **2015**, 5, 49623-49632.
10. J. W. Lee, J. Lee, C. Kim, C.-Y. Cho and J. H. Moon, Facile fabrication of sub-100 nm mesoscale inverse opal films and their application in dye-sensitized solar cell electrodes, Sci. Rep., **2014**, 4, 6804.
11. J. W. Lee and J. H. Moon, Monolithic multiscale bilayer inverse opal electrodes for dye-sensitized solar cell applications, Nanoscale, **2015**, 7, 5164-5168.
12. M. D′ Arienzo, L. Armelao, A. Cacciamani, C. M. Mari, S. Polizzi, R. Ruffo, R. Scotti, A. Testino, L. Wahba and F. Morazzoni, One-step preparation of SnO_2 and Pt-doped SnO_2 As Inverse Opal thin films for gas sensing, Chem. Mater., **2010**, 22, 4083-4089.
13. Y. Xie, R. Q. Xing, Q. L. Li, L. Xu and H. W. Song, Three-dimensional ordered ZnO-CuO inverse opals toward low concentration acetone detection for exhaled breath sensing, Sens. Actuators B, **2015**, 211, 255-262.
14. T. S. Wang, X. Y. Kou, L. P. Zhao, P. Sun, C. Liu, Y. Wang, K. Shimanoe, N. Yamazoe and G. Y. Lu, Flower-like ZnO hollow microspheres loaded with CdO nanoparticlesas high performance sensing material for gas sensors, Sens. Actuators B, **2017**, 250, 692-702.
15. X. Xue, L. Xing, Y. Chen, S. Shi, Y. Wang and T. Wang, Synthesis and H_2S sensing properties of CuO-SnO_2 core/shell pn-junction nanorods, J. Phys. Chem. C, **2008**, 112, 12157.
16. M. Bao, Y. J. Chen, F. Li, J. M. Ma, T. Lv, Y. J. Tang, L. B. Chen, Z. Xu and T. H. Wang, Plate-like p-n heterogeneous NiO/WO_3 nanocomposites for high performance room temperature NO_2 sensors, Nanoscale, **2014**, 6, 4063-4066.
17. J. M. Suh, Y.-S. Shim, D. H. Kim, W. Sohn, Y. Jung, S. Y. Lee, S. Choi, Y. H. Kim, J.-M. Jeon, K. Hong, K. C. Kwon, S. Y. Park, C. Kim, J.-H. Lee, C.-Y. Kang and H. W. Jang, Synergetically selective toluene sensing in hematite-decorated nickel oxide nanocorals, Adv. Mater. Technol., **2017**, 2, 1600259.
18. B. Wu, Z. Q. Lin, M. Q. Sheng, S. Y. Hou and J. F. Xu, Visible-light activated ZnO/CdSe heterostructure-based gas sensorswith low operating temperature, Appl. Surf. Sci., **2016**, 360, 652-657.
19. P. Camagni, G. Faglia, P. Galinetto, C. Perego, G. Samoggia and G. Sberveglieri, Photosensitivity activation of SnO_2 thin film gas sensors at room temperature, Sens. Actuators B, **1996**, 31, 99-103.
20. L. F. D. Silva, J.-C. M′ Peko, A. C. Catto, S. Bernardini, V. R. Mastelaro, K. Aguir, C. Ribeiro and E. Longo, UV-enhanced ozone gas sensing response of ZnO-SnO_2 heterojunctions at room temperature, Sens. Actuators B, **2017**, 240, 573-579.
21. G. Y. Lu, J. Xu, J. B. Sun, Y. S. Yu, Y. Q. Zhang and F. M. Liu, UV-enhanced room temperature NO_2 sensor using ZnO nanorods modified with SnO_2 nanoparticles, Sens. Actuators B, **2012**, 162, 82-88.
22. E. Espid and F. Taghipour, Development of highly sensitive ZnO/In_2O_3 composite gas sensoractivated by UV-LED, Sens. Actuators B,

View Article Online
DOI: 10.1039/C7NR08366A

2017, 241, 828-839.
23. Y. H. Gui, S. M. Li, J. Q. Xu and C. Li, Study on TiO_2-doped ZnO thick film gas sensors enhanced by UV light at room temperature, Microelectronic J., **2008**, 39, 1120-1125.
24. N. Wei, H. Z. Cui, X. Z. Wang, X. Xie, M. L. Wang, L. Q. Zhang and J. Tian, Hierarchical assembly of In_2O_3 nanoparticles on ZnO hollow nanotubes using carbon fibers as templates: Enhanced photocatalytic and gas sensingproperties, J. Colloid Interf. Sci., **2017**, 498, 263-270.
25. Z. Yang, L. J. Guo, B. Y. Zu, Y. N. Guo, T. Xu and X. C. Dou, CdS/ZnO core/shell nanowire-built films for enhanced photodetecting and optoelectronic gas-sensing applications, Adv. Optical Mater., **2014**, 2, 738-745.
26. L. N. Han, D. J. Wang, J. B. Cui, L. P. Chen, T. F. Jiang and Y. H. Lin, Study on formaldehyde gas-sensing of In_2O_3-sensitized ZnO nanoflowers under visible light irradiation at room temperature, J. Mater. Chem., **2012**, 22, 12915-12920.
27. J.-W. Yoon, S. H. Choi, J.-S. Kim, H. W. Jang, Y. C. Kang and J.-H. Lee, Trimodally porous SnO_2 nanospheres with three dimensional interconnectivity and size tunability: a one-pot synthetic route and potential application as an extremely sensitive ethanol detector, NPG Asia Mater., **2016**, 8, e244.
28. M. Yang, J. Ma, C. L. Zhang, Z. Z. Yang and Y. F. Lu, General synthetic route toward functional hollow spheres with double-shelled structures, Angew. Chem. Int. Ed., **2005**, 44, 6727-6730.
29. A. A. Firooz, T. Hyodo, A. R. Mahjoub, A. A. Khodadadi and Y. Shimizu, Synthesis and gas-sensing properties of nano- and meso-porous MoO_3-doped SnO_2, Sens. Actuators B, **2010**, 147, 554-560.
30. T. Hyodo, H. Inoue, H. Motomura, K. Matsuo, T. Hashishin, J. Tamaki, Y. Shimizu and M. Egashira, NO_2 sensing properties of macroporous In_2O_3-based powders fabricated by utilizing ultrasonic spray pyrolysis employing polymethylmethacrylate microspheres as a template, Sens. Actuators B, **2010**, 151, 265-273.
31. G. K. Pradhan, D. K. Padhi and K. M. Parida, Fabrication of α-Fe_2O_3 nanorod/RGO composite: a novel hybrid photocatalyst for phenol degradation, ACS Appl. Mater. Inter., **2013**, 5, 9101-9110.
32. S. Martha, K. H. Reddy and K. M. Parida, Fabrication of In_2O_3 modified ZnO for enhancing stability, optical behaviour, electronic properties and photocatalytic activity for hydrogen production under visible light, J. Mater. Chem. A, **2014**, 2, 3621-3631.
33. Z. Y. Wang, B. B. Huang, Y. Dai, X. Y. Qin, X. Y. Zhang, P. Wang, H. X. Liu and J. X. Yu, Highly photocatalytic ZnO/In_2O_3 heteronanostructures synthesized by a coprecipitation method, J. Phys. Chem. C, **2009**, 113, 4612-4617.
34. S. Pati, S. B. Majumder and P. Banerji, Role of oxygen vacancy in optical and gas sensing characteristics of ZnO thin films, J. Alloy Compd., **2012**, 541, 376-379.
35. G. Singh, A. Choudhary, D. Haranath, A. G. Joshi, N. Singh, S. Singh and R. Pasricha, ZnO decorated luminescent graphene as a potential gas sensor at room temperature, Carbon, **2012**, 50, 385-394.
36. F. Zhang, X. Y. Li, Q. D. Zhao, Q. Z. Zhang, M. Tadé and S. M. Liu, Fabrication of a-Fe_2O_3/In_2O_3 composite hollow microspheres: A novel hybrid photocatalyst for toluene degradation under visible light, J. Colloid Interf. Sci., **2015**, 457, 18-26.
37. C. Q. Wang, D. R. Chen, X. L. Jiao and C. L. Chen, Lotus-root-like In_2O_3 nanostructures: fabrication, characterization, and photoluminescence properties, J. Phys. Chem. C, **2007**, 111, 13398-13403.
38. M. Gholami, A. A. Khodadadi, A. A. Firooz and Y. Mortazavi, In_2O_3-ZnO nanocomposites: High sensor response and selectivity to ethanol, Sens. Actuators B, **2015**, 212, 395-403.
39. J.-W. Yoon, J.-S. Kim, T.-H. Kim, Y. J. Hong, Y. C. Kang and J.-H. Lee, A New Strategy for Humidity Independent Oxide Chemiresistors: Dynamic Self-Refreshing of In_2O_3 Sensing Surface Assisted by Layer-by-Layer Coated CeO_2 Nanoclusters, Small, **2016**, 12, 4229-4240.
40. N. Barsan and U. Weimar, Conduction model of metal oxide gas sensors, J. Electroceram., **2001**, 7, 143.
41. S. W. Fan, A. K. Srivastava and V. P. Dravid, UV-activated room-temperature gas sensing mechanism of polycrystalline ZnO, Appl. Phys. Lett., **2009**, 95, 142106.
42. A. Nashim, S. Martha and K. M. Parida, $Gd_2Ti_2O_7$/In_2O_3: efficient visible-light-driven heterojunction-based composite photocatalysts for hydrogen production, ChemCatChem., **2013**, 8, 2352-2359.
43. S. Martha, K. H. Reddy and K. M. Parida, Fabrication of In_2O_3 modified ZnO for enhancing stability, optical behaviour, electronic properties and photocatalytic activity for hydrogen production under visible light, J. Mater. Chem. A, **2014**, 2, 3621.
44. G.-J. Lee, S. Anandan, S. J. Masten and J. J. Wu, Photocatalytic hydrogen evolution from water splitting using Cu doped ZnS microspheres under visible light irradiation, Renew. Energ., **2016**, 89, 18e26.

View Article Online
DOI: 10.1039/C7NR08366A

Table of Contents Entry

Rational Design of 3D Inverse Opals Heterogeneous Composites Microspheres as Excellent Visible-Light-Induced NO_2 Sensor at Room Temperature

Tianshuang Wang, Qi Yu, Sufang Zhang, Xueying Kou, Peng Sun* and Geyu Lu*

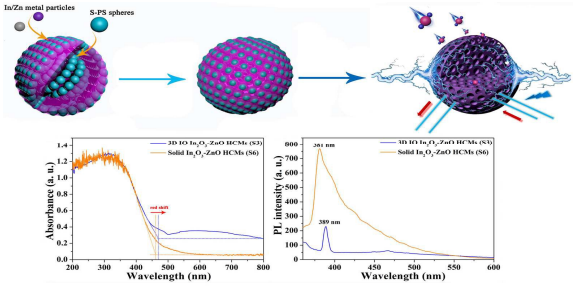

We provide a novel strategy for fabricating 3D IO heterogeneous composites microspheres and achieve detection of NO_2 at room temperature